1 OF 1

AD
A031407

END

DATE
FILMED

12-76

MICROCOPY RESOLUTION TEST CHART
NATIONAL BUREAU OF STANDARDS-1963-A

FC (12)
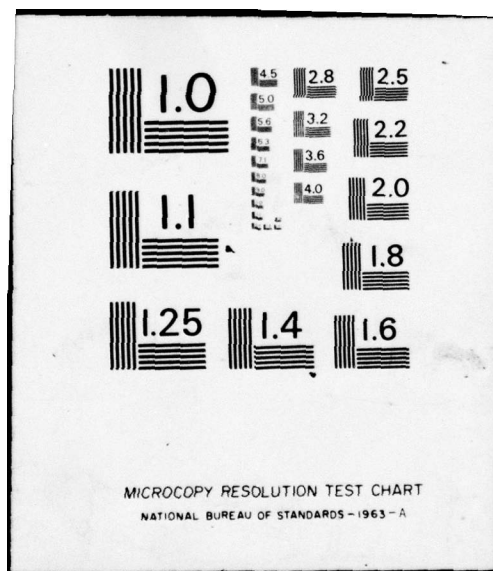
SC5023.9TR

COPY NO. 16

IMPACT DAMAGE IN BRITTLE MATERIALS

IN THE PLASTIC RESPONSE REGIME

Technical Report

1st Jan. 1976 thru 30 Oct. 1976
Contract No. N00014-75-C-0669
Project No. 471

Submitted to:

Office of Naval Research
800 N. Quincy Street
Arlington, VA 22217

Reproduction in Whole or in Part is Permitted for
any purpose of the United States Government

NOV 1 1976

Science Center
Rockwell International

SECURITY CLASSIFICATION OF THIS PAGE *(When Data Entered)*

REPORT DOCUMENTATION PAGE		READ INSTRUCTIONS BEFORE COMPLETING FORM
1. REPORT NUMBER	2. GOVT ACCESSION NO.	3. RECIPIENT'S CATALOG NUMBER
4. TITLE *(and Subtitle)* IMPACT DAMAGE IN BRITTLE MATERIALS IN THE PLASTIC RESPONSE REGIME.		5. TYPE OF REPORT & PERIOD COVERED Technical Jan 1, 1976 thru Oct. 30, '76
		6. PERFORMING ORG. REPORT NUMBER SC5023-9TR
7. AUTHOR(s) A. G. Evans, M. E. Gulden, G. E. Eggum and M. Rosenblatt		8. CONTRACT OR GRANT NUMBER(s) N00014-75-C-0669
9. PERFORMING ORGANIZATION NAME AND ADDRESS Rockwell International Science Center Thousand Oaks, CA 91360		10. PROGRAM ELEMENT, PROJECT, TASK AREA & WORK UNIT NUMBERS Project No. 471
11. CONTROLLING OFFICE NAME AND ADDRESS Office of Naval Research 800 N. Quincy Street Arlington, VA 22217 (Code 471)		12. REPORT DATE Oct. 30, 1976
		13. NUMBER OF PAGES 54
14. MONITORING AGENCY NAME & ADDRESS *(if different from Controlling Office)*		15. SECURITY CLASS. *(of this report)* Unclassified
		15a. DECLASSIFICATION/DOWNGRADING SCHEDULE

16. DISTRIBUTION STATEMENT *(of this Report)*

Approved for Public Release; distribution unlimited

17. DISTRIBUTION STATEMENT *(of the abstract entered in Block 20, if different from Report)*

18. SUPPLEMENTARY NOTES

19. KEY WORDS *(Continue on reverse side if necessary and identify by block number)*

Impact, erosion, ceramics, projectiles, toughness, hardness

20. ABSTRACT *(Continue on reverse side if necessary and identify by block number)*

The impact damage created in the plastic response regime has been characterized in terms of the surface extension and the penetration of the fractures. A numerical dynamic analysis has been performed (of a typical impact within this regime) to indicate some of the principal characteristics of the contact behavior and the stress field. The damage has then been analyzed - using simplified postulates based on key features of the impact dynamics and the quasi-static indentation fracture - which has enabled the primary material and target parameters affecting the impact fracture to be identified. Thereafter, some implications for strength

DD $_{1\ JAN\ 73}^{FORM}$ 1473   EDITION OF 1 NOV 65 IS OBSOLETE

SECURITY CLASSIFICATION OF THIS PAGE *(When Data Entered)*

degradation and erosion have been discussed.

TABLE OF CONTENTS

IMPACT DAMAGE IN BRITTLE MATERIALS

IN THE PLASTIC RESPONSE REGIME

by

A. G. Evans

Science Center, Rockwell International
Thousand Oaks, CA 91360

M. E. Gulden

Solar, San Diego, CA 92101

and

G. E. Eggum, M. Rosenblatt

California Research and Technology
Woodland Hills, CA 91367

ABSTRACT

The impact damage created in the plastic response regime has been characterized in terms of the surface extension and the penetration of the fractures. A numerical dynamic analysis has been performed (of a typical impact within this regime) to indicate some of the principal characteristics of the contact behavior and the stress field. The damage has then been analyzed - using simplified postulates based on key features of the impact dynamics and the quasi-static indentation fracture - which has enabled the primary material and target parameters affecting the impact fracture to be identified. Thereafter, some implications for strength degradation and erosion have been discussed.

1.0 INTRODUCTION

Previous studies of the damage in brittle materials produced by quasi-static indentation[1,2] and by the impact of relatively incompressible projectiles[3] have shown that plastic indentation of the target is accompanied by very specific modes of fracture (Fig. 1). The two primary types of fracture are 'radial' cracks (radius C_r) that propagate radially outward from the contact zone, and 'lateral' cracks (radius C_ℓ) that initiate beneath the contact zone and propagate between the radial cracks on planes nearly parallel to the surface. The former are the prime source of strength degradation, whereas the latter are a potential source of material removal. The primary objective of the present paper is to examine in detail the fractures produced in this regime by the impact of solid projectiles, in order to deduce relationships between the magnitude of the fractures and the properties of the target and projectile.

The study is in three principal parts. Firstly, observations and measurements of the fractures produced in a range of ceramic targets by several projectiles (Table I)[‡]; then, a numerical analysis of certain aspects of the projectile impact process; and finally, an analysis of the damage (based on an interpretation of the measurements and stress analysis) which develops the requisite relations between the damage and the material properties. Thereafter, some implications of the fracture characterization for several problems of practical concern (such as erosion and strength degradation) are discussed.

2.0 DAMAGE OBSERVATIONS AND MEASUREMENTS

2.1 Experimental Techniques

[‡] Also included in Table I are the pertinent physical properties of the materials. The hardnesses are standard quasi-static Vickers values obtained in the load independent regime, the toughnesses were determined using the indentation technique,[4] and the moduli and acoustic impedances were determined using conventional acoustic methods.

The impact experiments were conducted using two techniques; a single particle exploding foil method,[5] and a multiparticle gas stream method.[6] The former is restricted to projectiles larger than ~ 400 μm in diameter, but has an essentially unlimited velocity capability (1000 ms^{-1} was the maximum velocity used in the present study); while the latter is capable of using very small particles (angular or spherical) but is confined to velocities $\gtrsim 300$ ms^{-1}. The two methods were thus quite complementary and, when used in coordination, permitted a wide range of impact conditions to be evaluated. All tests were conducted on samples with a minimum dimension $\gtrsim 50$ times the projectile diameter, to avert damage being induced by stress waves reflected from the sample boundaries. The impact damage was observed using optical and electron microscopy, on both the impacted surfaces and on orthogonal sections through the impact center.

2.2 Observations

a) Impact Surface

The damage pattern observed on the impacted surfaces were, in all cases, essentially similar to those depicted in Fig. 1, i.e. consisting of radial and lateral cracks. However, damage features of special interest are summarized in Figs. 2, 3 and 4. The fractures created by angular particles (Figs. 2a,b) are similar in form to those produced by spherical particles (Fig. 1), but exhibit asymmetries that depend on the geometry of the contact zone. Multiparticle tests (Figs. 2,3) indicate that the interaction between adjacent impact sites occurs only when the separation (r_c) of the impact centers approaches the sum ($2 C_\ell$) of the lateral crack extensions at each impact site (as predicted by quasi-static indentation studies[1]); Fig. 2a is an example of the interaction of two adjacent impacts at $r_c < 2 C_\ell$), and Fig. 3a provides an example of non-interacting impacts at r_c only slightly larger than $2 C_\ell$. The condition of the surface does not appear to have a significant effect on the mode of fracture, because similar

4

fracture characteristics are observed on polished surfaces (Fig. 3a) and on pre-damaged surfaces (Fig. 3b). Finally, the damage patterns observed on target materials with a quasi-static hardness larger than the projectile (Fig. 4) are of considerable interest. The target still responds plastically, as indicated by the zones of birefringence (Fig. 4c). However, whereas at high velocities (Fig. 4d) the damage is essentially the same as that encountered in the softer target materials (Fig. 1d), at low and intermediate velocities the zone of permanent deformation indicated by scanning electron microscopy (Fig. 4b) is substantially smaller than the total contact zone suggested by transmission optical microscopy (Fig. 4a) (an equivalent disparity does not exist for the softer target materials, Figs. 1a, b).

b) Orthogonal Sections

The sub-surface damage, as manifested on orthogonal sections, is summarized in Figs. 5,6. In all cases, the damage consists of a series of radial cracks that penetrate into the target to a distance approximately equal to their surface extension, and a series of lateral cracks that, although exhibiting a considerable length variability, have a maximum extension similar to the extension of the radial cracks. The intensity of the damage (i.e. the total number of radial and, especially, lateral cracks) is much greater for the soft materials (Fig. 5) than for the hard (or tough) materials (Fig. 6). The shape of the damage zone also exhibits some dependence on the projectile; namely, for high impedance projectiles (e.g. WC), the damage is intense, the material removal is large and the lateral cracks tend to incline toward the target surface (Fig. 5a,b), whereas for lower impedance projectiles (e.g. glass) the damage is less intense, the material removal is minimal and the lateral cracks tend to extend almost parallel to the surface (Fig. 5c,d). Two additional features to note are; (i) the frequent initiation of lateral fractures at radial cracks (e.g. at A in Fig. 5b) indicating that the radial cracks were the first to form (c.f.

5

quasi-static indentation, (ii) the occurrence of a zone of microfracture beneath the impression (Fig. 5d) suggestive of a plastic zone with microcracks induced by unaccommodated localized deformation.

2.3 Damage Measurements

a) Radial Cracks

The average lengths, C_r, of the radial cracks were determined for each experiment. These results are summarized in Table II. It is immediately apparent from the data that, for a given projectile, the crack lengths are almost directly proportional to the projectile velocity; this feature is illustrated in Fig. 7 for some of the data obtained on ZnS, Si_3N_4 and MgF_2. Also, as noted in a previous study,[3] the crack lengths are much larger than those obtained quasi-statically for the equivalent impression radius, a (Fig. 8).

b) Lateral Cracks

The lateral cracks are a highly variable entity; but the maximum depth, h, at which significant lateral fracture can be detected beneath the contact center appears to vary in a systematic manner. A summary of these damage penetration measurements is presented in Table III. Careful examination of these results, plus plastic impression data (see Fig. 8), indicates that h correlates directly with the impression radius. This is illustrated in Fig. 9 for the data obtained on ZnS.

c) Fracture Threshold

There are insufficient data to clearly delineate the fracture threshold, although several observations (e.g. Fig. 10) have indicated that such a threshold exists for all target materials. Approximate threshold velocities deduced from the present damage observations are summarized in Table IV.

3.0 DYNAMIC ANALYSIS

The numerical analysis was performed using the WAVE-L code, which is a Lagrangian finite difference code of the Hemp type.[7] In such analyses, the continuum of interest, which may include material interfaces or free surfaces, is initially divided into a number of volume elements, or cells, each of which has a set of stresses, velocities, etc., associated with it. These quantities are then updated in a stepwise fashion (each step, or cycle, representing an increment in time), and the dynamic behavior of the system is thereby determined.

The equations for updating the cell variables during a time cycle are obtained from the finite difference analogs of the differential equations expressing conservation of mass, conservation of momentum, conservation of energy, and the constitutive relationships for the materials being analyzed. In Lagrangian type codes, the computational cells always enclose the same element of mass, thereby ensuring that the integrity of material interfaces is maintained. (In Eulerian codes the grid network is stationary, and the mass flows across cell boundaries.)

The WAVE-L code can accommodate constitutive properties of a very general nature; in the present analysis an elastic-perfectly plastic material was assumed with a Von Mises yield criterion. The yield stress ($\sigma_y = 2GNm^{-2}$) was chosen to match modified indentation data[‡] for ZnS which specifies the average force on the indenter as a function of the contact radius.[2]

The material interface between the projectile and the target was treated as friction free, i.e., no shear stresses were allowed on the interface, and the projectile was considered to be a rigid sphere. These simplifications were used to eliminate extensive rezoning of the heavily deformed region near the interface.

[‡] The measured quasi-static indentation force for ZnS[2] was increased by ~ 50% to make approximate allowance for the strain-rate sensitivity of the plastic flow stress.[3]

However, the latter excludes possible effects of stress wave reflections in the projectile (the significance of this simplification is discussed below in more detail). The motion of the indenter was calculated by integrating the stresses acting on the surface of the indenter to obtain the total force, and dividing by the mass to obtain the acceleration. This was then integrated to obtain the velocity.

The principal results of the dynamic analyses are summarized in Figs. 11-13. The contact pressure, p, (Fig. 11a) decreases rapidly from an initial value of $\sim p_0$ (the one dimensional contact pressure given by eqn 4) and then becomes nearly constant at a time, t_1 (Fig. 11a) which essentially coincides with the time when the plastic wave front moves ahead of the expanding interface, i.e. when the plastic zone detatches from the projectile surface. Note, however, that the super-position of intra-projectile stress wave reflections could cause the pressure to be reduced below that in Fig. 11a at times $\gtrsim t_p$, the stress wave transit time in the projectile (c.f. the one-dimensional analogy[3,8]). The contact radius increases monotonically (Fig. 11b) in approximate accord with a square root depen-dence on time ($a \cong \sqrt{t}$); although again, the increase could be overestimated at times $\gtrsim t_p$. During the penetration phase, the plastic wave continues to propagate (Fig. 12). The stresses within the plastic zone are compressive; while outside the plastic zone (Fig. 13a,b) the stresses (both radial and tangential) are tensile, and nearly symmetric about the center of contact, 0. After full penetration, the unloading generates additional tensile stresses (Fig. 13c,d) within both the elastic and plastic zones (a one-dimensional analogy is the tensile stress generation that occurs when the unloading elastic wave interacts with the slower moving plastic wave[9]), with the maximum occurring in the elastic zone close to the elastic/plastic interface.

4.0 DAMAGE ANALYSIS

The complexity of the dynamic stress fields (section 3), and the intractability of pertinent dynamic crack propagation analyses, preclude an effective damage analysis based on the details of the stress field. Hence, the approach adopted in the present study is to postulate simplified (but plausible) crack propagation characteristics, using the dynamics of section 3 and the quasi-static indentation fracture characteristics[2,4] for guidance. Then functional forms of the fracture relations, implied by these postulates, are derived and compared with the fracture data. When consistency is established, the basic premise is considered to be essentially valid, and more refined analysis might then be initiated. This 'semi-empirical' approach is implemented herein by firstly considering the development of the radial cracks (see section 2), and then evaluating the subsequent formation of the lateral cracks.

4.1 Radial Cracks

The driving force for crack extension during projectile impact is the dynamic tensile stress field, and the resistance to crack propagation is determined by the fracture toughness of the material, K_c. The relation between the crack radius, C_r, and the dynamic stress and toughness parameters can be expressed in normalized form[2] by;

$$\frac{K_c}{\sigma_p(t_a)\sqrt{a}} = f_1\left(\frac{a}{C_r}\right) \int_{-C_r/a}^{C_r/a} f_2\left[(C/a),\ (r/a)\right] f_3[r/a, r_y/a]d(r/a) \tag{1}$$

where a is the contact radius, σ_p is the peak value of the tensile stress at the instant (t_a) of crack arrest, r is the distance from the center of contact and r_y is the distance between the plastic wave front and the contact center: f_1, f_2 and f_3 are functions, with f_1 and f_2 being conventional terms that depend on the geometry of the crack, e.g. for a penny-crack[10]

9

$$f_1 = \left(\frac{a}{\pi C_r}\right)^{3/2}$$

$$f_2 = \frac{(r/a)\sqrt{1 - [(r/a)/(C_r/a)]^2}}{\left[1 - (r/a)/(C_r/a)\right]^2} \tag{2}$$

while f_3 describes the spatial dependence of the tensile stress at time t_a.

An empirical evaluation of the <u>quasi-static</u> radial crack extension[2] (predicated on the presence of tangential tensile stresses) has shown that eqn (1) reduces, in that case, to;

$$\frac{C_r}{a} \approx F_1\left(\frac{p\sqrt{a}}{K_c}\right) \tag{3a}$$

where p is the contact pressure and, at $C_r/a \gtrsim 3$;

$$F_1 = \kappa \left(\frac{p\sqrt{a}}{K_c}\right)^{2/3}, \tag{3b}$$

where κ is a dimensionless constant. The effect of the contact pressure arises because the stress <u>amplitude</u> scales primarily with p, and the influence of the contact radius stems from its effect of the <u>spatial extension</u> of the stress field.

Similar tangential stresses develop during the early stages of impact (Fig. 13). Therefore, a plausible preliminary postulate might propose that the impact radial fractures form during penetration, and exhibit an analogous dependence on the contact pressure and the contact radius[‡]. It follows from this postulate that the final crack length should be related to a maximum value of some product of p and a, with the exact form of this product depending on the dynamic equivalent of F_1.

[‡] In fact, the dynamic stress that result from the impact of an elastic half space by a deformable projectile[11] has already been suggested to exhibit an equivalent dependence on p and a.

10

The contact pressure (Fig. 11a) has a peak value, p_o, at initial contact given at relatively low velocities ($\gtrsim 3000$ ms^{-1}) by the approximate one dimensional result,[3,8]

$$p_o \approx z_t \, \Delta u_p \equiv \frac{v_o z_t z_p}{z_p + z_t} \tag{4}$$

where Δu_p is the discontinuity in particle velocity upon impact, v_o is the projectile velocity and z_t and z_p are the acoustic impedances of the target and projectile, respectively. In general, $p = \alpha p_o$ where α is a dimensionless variable that depends on several properties of the target and projectile. The contact radius, a, increases with time (Fig. 11b), and for a relatively rigid projectile, a, is related to the plastic penetration, q, by[3]

$$\frac{a}{R_p} = \sqrt{\frac{2q}{R_p} - \left(\frac{a}{R_p}\right)^2} \qquad (q \lesssim R) \tag{5}$$

But, the plastic penetration is related to the mean interface velocity $\bar{u}_i (q = \bar{u}_i t)$, which has a peak value (u_o) immediately after initial contact, given by the approximate one-dimensional result;[3,8]

$$u_o \approx \frac{v_o z_p}{z_t + z_p} \tag{6}$$

In general, $u_i = \beta u_o$, where β is a dimensionless variable.

In order to interrelate eqns (4), (5) and (6) to obtain an estimate of the crack extension from eqn (3), it is now required to define a critical time, t_c, at which the pertinent product of p and a reaches a maximum. For the one-dimensional analogy,[3,8] this critical time would probably coincide with the return of the longitudinal stress wave in the projectile to the contact interface -- an event which produces a substantial discontinuity in the contact pressure -- giving

$$t_c = \frac{4R_p}{c_p} \tag{7}$$

11

where c_p is the longitudinal wave speed in the projectile. A similar character-istic time may also pertain in the three-dimensional projectile impact problem; it would not coincide with a discontinuity in the contact pressure, but may signify the onset of a relatively rapid pressure decay. Alternately, since the contact interface expands quite rapidly during a projectile impact, a significant change in the pressure variation might occur when the elastic or plastic wave front first moves ahead of the expanding interface to reach the free surface: the characteristic time for this event derives from the penetration (eqn 5) and the wave velocity in the target (c) as;

$$t_c = \frac{2 R_p}{\bar{u}_i [1 + (c/\bar{u}_i)^2]} \tag{8}$$

Note that in both cases the characteristic time is directly proportional to the projectile radius and inversely proportional to a characteristic velocity (in fact, this effect is likely to be quite general). The present impact analysis (section 3) does not indicate a pressure decrease corresponding to either of the stress wave events within the target (rather, the pressure appears to stabilize after the passage of the plastic wave front). The reflected stress wave charac-teristic for the projectile is thus used for preliminary evaluation. The contact radius, a_c, at the critical time then becomes

$$a_c = R_p \sqrt{\beta v_o \xi (2 - \beta v_o \xi)} \tag{9}$$

where $\xi = 4z_p/[(z_t + z_p)c_p]$.

A final result for the crack length can now be obtained by inserting p and a_c into eqn (3). For the specific form of F_1 given by eqn (3b)[‡];

[‡] This form might, in fact, be quite reasonable for the dynamic problem at large C_r/a, because the spatial stress field variation, $\sim 1/r^2$ (i.e. the attenuation due to a spherically expanding stress wave), is essentially the same as that for the quasi-static problem (as given by the Boussinesq result[2]).

$$\frac{C_r}{v_o} \approx \left(\frac{R_p^2}{K_c}\right)^{1/3} z_t^{2/3} \sqrt{2 - \beta v_o \xi} \tag{10a}$$

where λ is a composite of α, β and ξ. This result can also be expressed in a more general form, that should apply for any F_1 or t_c, as;

$$\frac{C_r}{v_o} = \Phi_1 \left(\frac{R_p^2}{K_c}\right) \Phi_2 (z_t) \; \Phi_3 [v_o, z_p, c(c_p)] \tag{10b}$$

where the Φ are undetermined functions. At this juncture, it is noted that an interesting similarity exists between the radial crack lengths predicted by the present dynamic analysis and the connical (Hertzian) crack lengths (C_c) predicted by a quasi-static fully elastic impact analysis (see Appendix);

$$\frac{C_c}{v_o} = A_3 \left(\frac{R_p^2}{K_c}\right)^{1/3} \left[\frac{\rho_p^6}{v_o^3 (E_p + E_t)^4}\right]^{1/15} \tag{10c}$$

This similarity is perhaps, less surprising, when it is recognized that the connical crack extension was also derived on the premise that the fracture is predicated on a maximum in the product of the pressure and contact radius (equivalent, in this case, to a maximum in the force). The consequences of this similarity will be examined later.

The essence of the present postulate is its inference that the prime target parameters affecting the radial fracture are the fracture toughness and, perhaps, the acoustic impedance (note that the dynamic plastic properties are relatively unimportant, only entering Φ_3 as a possible secondary factor through the plastic wave velocity, c), while the important projectile parameters are the radius and velocity. The utility of the postulate can thus be assessed by comparing these predictions with impact damage data.[‡] It has already been established that,

---

[‡] The form of eqn (10b) is perhaps sufficiently general that other postulates would yield an equivalent result. However, the specific forms (eqns 10a,c) are unlikely to result from alternate postulates, and thus afford a stringent test of the utility of the present approach.

within the present range of test velocities ($\tilde{>} 1000$ ms^{-1}), the radial crack size scales directly with the projectile velocity, as shown in Fig. 7.[‡] Hence, hereafter, normalized crack lengths (C_r/v_0) are used to characterize the radial fracture.

The effect of the projectile radius is plotted in Fig. 14 for a range of projectiles (both spherical and angular) and four target materials (ZnS, MgO, MgF$_2$ and Mg$_2$Al$_2$O$_4$) with similar values of acoustic impedance (3×10^7 kgm^{-2}s^{-1}) and toughness (~ 1 MPa$\sqrt{m}$), but widely different propensities for plastic flow (H = 2 - 16 GNm^{-2}), as summarized in Table I. The conformity of the fracture data (within a factor of 2 in C_r/v_0) indicates that the plastic properties of the target and the shape (and properties) of the projectile are of secondary importance, as inferred by the present postulate. The plot also emphasizes the anticipated primary role of the projectile radius   (an experimental exponent of 1.5 compared with a predicted exponent of 1.3).

The effect of the fracture toughness on the damage is demonstrated in Fig. 15 where the normalized crack lengths for silicon nitride are compared with the data line for the preceding four materials. Silicon nitride has an acoustic impedance essentially similar to the other materials and a hardness similar to spinel, but a much larger toughness (~ 5 MPa $\sqrt{m}$). The factor of ~ 4 reduction in crack extension for equivalent projectile conditions must be attributed to the larger toughness, again consistent with the general predictions of the postulate and the specific predictions of eqn (10). The combined effect of toughness and impedance is also indicated on Fig. 15 by the tungsten carbide data. The normalized crack length is not quite as small as anticipated from the large toughness of WC (13 MPa$\sqrt{m}$). Some counteractive effect is thus in evidence; this is likely to be associated with the high impedance of the WC, as predicted by eqn (10), but

---

[‡] However, note that eqns (10a,b) indicate some deviation from this behavior at higher velocities, as Φ_3 becomes significantly dependent on the velocity.

14

the effect is minor.

An approximate relation for the radial crack extension, derived from
the present test data, that incorporates the primary target and projectile
parameters is thus;

$$\frac{C_r}{v_0} \approx \lambda \left(\frac{R_p^2}{K_c}\right)^{3/4} \tag{11}$$

where λ is a parameter that exhibits some dependence on the acoustic impedances
of the target and projectile.

The extent of the radial fracture produced by the impact of solid
projectiles at relatively low velocities ($\gtrsim 1000$ ms^{-1}) thus appears to be
primarily dependent on the fracture toughness of the target, and on the radius
and velocity of the projectile. These dependencies were developed from a postu-
late which specifies that the radial fractures are created at a relatively early
stage in the impact process, when a product of the contact pressure (which pre-
sumably determines the magnitude of the dynamic tensile stresses) and the contact
radius (which dictates the spatial extension of the stress field) reach a maximum.
The consistency of the test data with the expectations of this postulate[‡] suggests,
but does not necessarily verify, that the postulate provides an effective des-
cription of the radial fracture process. At higher projectile velocities, the
nature of the damage is expected to be similar, but the functional dependencies
on the important target and projectile parameters may differ from those presented
in Figs. 14, 15.

4.2 Lateral Cracks

The formation and growth of the lateral cracks obtained in quasi-static
indentation has been attributed to the residual stress that develops from plastic

---

[‡] It is interesting to note the data, in fact, correlate more closely with the
quasi-static elastic result (eqn 10c) which predicts a small dependence on
the impedance of the target.

penetration in an elastic/plastic solid.[1,2] Since the maximum residual tensile stresses occur within the vicinity of the plastic zone, the zone of lateral fracture might, therefore, be anticipated to exhibit some dependence on the plastic zone radius, r_y. Two additional factors suggest, in fact, that the depth of the lateral fractures, h, produced by projectile impact might be approximately equal to the maximum depth of the plastic zone (i.e. the zone depth at full penetration). Firstly, the in-plane tensile stresses (for the impact problem presented in section 3) exhibit a maximum near the elastic/plastic inter-face (Fig. 13c,d), after full penetration. Secondly, the impression radius is directly proportional to both the damage penetration, h (Fig. 9), and the plastic zone radius, r_y^2. Therefore, a plausible preliminary postulate states that the lateral fractures initiate within a zone that extends to the elastic/plastic interface at full penetration.

For penetrations less than the projectile radius, the penetration given by eqn (5), and the observed proportionality between h and a, yield;

$$h/R_p = \lambda' \sqrt{(q/R_p)[2 - (q/R_p)^2]} \tag{12}$$

where λ' is a dimensionless constant. The plastic penetration of projectiles has been estimated under a variety of penetration conditions[12] (using the equations of motion) to show that in general;

$$\frac{q}{R_p} = F_2 \left(v_o \sqrt{\frac{\rho_p}{\sigma_y}} \right) F_3 (n) F_4 (\rho_t) \tag{13}$$

where ρ_p and ρ_t are the densities of the projectile and target, respectively, σ_y is the 'yield stress' that pertains at the full penetration condition, n is a 'work hardening' exponent, and the F are functions shown in Fig. 16. F_4 is a target inertia term that only becomes important at relatively high projectile velocities, the term will thus be neglected for data analysis in the present

16

velocity regime. Also, since the penetration rate as the projectile approaches full penetration should be a small fraction of the initial projectile velocity, it may be possible to characterize the deformation (σ_y and n) at this stage by the quasi-static hardness, $H(q)$. Adopting this assumption and neglecting work hardening, a comparison of eqns (12) and (13) gives

$$h/R_p = \Phi_4 \left(v_0 \sqrt{\frac{\rho_p}{H}} \right) \tag{14}$$

where Φ_4 is a function. The damage penetration data are plotted in the form suggested by eqn (14) in Fig. 17. It is apparent from the good consistency of the data that the normalized damage is indeed dictated primarily by $v_0 \sqrt{\rho_p/H}$ (although there are minor inconsistencies that are probably accounted for by secondary dependencies on other variables), such that;

$$(h/R_p)^2 \approx \lambda^* v_0 \sqrt{\rho_p/H} \tag{15}$$

where λ^* is a constant (≈ 3.5). Again, however, departures from this relatively simple behavior might arise at higher velocities where deep penetration or target inertial effects become important; although the same postulate, concerning the equivalence between the plastic zone at full penetration and the lateral fracture zone, may still apply.

4.3 Fracture Thresholds

The fracture threshold is an important aspect of the impact damage problem. Yet, even under quasi-static conditions this threshold is ill-defined and highly variable.[2] Analyses of indentation fracture[2,13] do not indicate the existence of a threshold, unless a statistical argument is invoked[2]; yet it is observed that plastic indentation of the surface of brittle materials can occur without crack formation, below specific projectile velocities (Fig. 10). However, a cursory examination of the approximate threshold data (Table IV) indicate that

the threshold condition increases as the toughness and/or hardness increase. This observation can be qualitatively explained if it is postulated that fracture initiation in a given material is related to a minimum penetration, q_c, such that q_c increases as the toughness of the material increases.[‡] A comparison of eqns (12) and (14) indicates that the penetration in the present velocity range is directly proportional to, $R_p v_o \rho_p / H$. Hence, an approximate fracture requirement, based on the present premise, is

$$v_o > \alpha^* \, \frac{H \, q_c \, (K_c)}{\rho_p \, R_p} \tag{16}$$

where α^* is a constant. The observed dependence of the threshold velocity on H and K_c is thus apparent, and an inverse dependence on the projectile density and radius appears, a tendency that can also be detected in the threshold data (Table IV). However, further studies are clearly needed to establish the merit of this description of the threshold.

5.0 IMPLICATIONS

5.1 Strength Degradation

The strength of the target material after impact is usually dominated by the radial cracks. Approximating these cracks to semi-circular surface cracks in a semi-infinite solid, the retained strength of the target, σ_R is simply;

$$\sigma_R = \frac{K_c}{2.1} \sqrt{\frac{\pi}{C_r}} \tag{17}$$

Hence, substituting the approximate functional relation for C_r from eqn (4) into eqn (13) enables σ_R to be expressed as;

[‡] A general behavior of this type seems to be consistent with observations of indentation fracture initiation in ceramic polycrystals (although there are some notable exceptions).

$$\sigma_R \approx \frac{\lambda'' \ K_c^{1.4}}{v_o^{0.5} \ R_p^{0.8}} \tag{18}$$

where λ'' is a constant. The primary target parameter affecting the strength degradation should thus be the fracture toughness; while the velocity and radius should be the key projectile parameters. Recent data on the strength degradation of glass[14] in the velocity regime where radial cracks are observed, confirm this predicted dependence of the retained strength on the projectile velocity and radius, as summarized in a plot of σ_R vs. $\left(v_o^{0.5} R_p^{0.8}\right)^{-1}$ (Fig. 18). The very important prediction of the dependence of the retained strength on the fracture toughness has not yet been tested. Data for the retained strength obtained at very low velocities, where connical rather than radial cracks are observed to form, are closely related to the data in the radial fracture regime,[14] consistent with our observation (section 4) that the dynamic and quasi-static regimes of impact fracture yield similar dependencies on the target and projectile parameters.

5.2 Erosion

Material removal in homogeneous ceramics is almost certainly related to the formation and growth of the lateral cracks. The maximum amount of material that could be removed per impact, $\hat{v}_i$, is thus the volume encompassed by the lateral cracks[2];

$$\hat{v}_i \approx \pi C_r^2 h \tag{19}$$

Substituting for C_r and h from eqns (11) and (15) thus gives;

$$\hat{v}_i \propto \frac{v_o^{2.5} R_p^{4.} \rho_p^{0.3}}{K_c^{1.5} H^{0.3}} \tag{20}$$

However, since the intensity of the lateral fracture also depends on certain material variables, M (notably the hardness and, perhaps, the toughness

19

- see section 2) the fraction of v_i actually removed per impact, X, could be a material dependent variable. The average amount of material removed per impact, $\bar{v}_i$, is thus;

$$\bar{v}_i \cong v_o^{2.5} R_p^4 \rho_p^{0.3} (1/HK_c^5)^{0.3} X (M) \qquad (21)$$

The importance of X can only be effectively evaluated by comparing the functional dependencies predicted by eqn (21) with erosion data obtained for a range of ceramic materials in the plastic response regime. An inventory of such data obtained for low velocity erosion (<200 ms^{-1}) by small (115 μm) quartz particles, and corresponding values for the important physical properties are summarized in Table V. The experimentally determined material removal per impact, normalized by $v_o^{2.5}$, is thus plotted in Fig. 19 as a function of $(1/K_c^5 H)$, which is the parameter in eqn (21) that contains the important target properties. There is a direct correlation of erosion rate with this variable. However, the dependence is greater than anticipated by eqn (21) (i.e. a best fit data slope of ~ 0.6 compared to a predicted slope of ~ 0.3), indicating that some of the dependence on K_c and H may derive from the X term and hence, that the erosion rate may not be uniquely defined by, $1/K_c^5 H$. Additional data are needed to establish the detailed correlation between the erosion rate and the target variables. One further feature of the erosion evaluation that should be noted concerns the data for the hot-pressed silicon nitride. The damage observations suggested that the response of this material to impacts by glass projectiles < 1000 μm in diameter was sub-threshold in character (Fig. 10) at velocities below ~ 1000 ms^{-1}. Hence, the erosion of this material by 115 μm glass particles at <200 ms^{-1} would undoubtedly be occurring by a different mechanism (i.e. that which applies below the fracture threshold), perhaps accounting for the much reduced erosion rate compared to that anticipated by extrapolation from the other materials. This feature illustrates the crucial importance of recognizing that more than one erosion mechanism exists and that

erosion rate predictions must firstly identify the pertinent erosion regime.

6.0 CONCLUSION

The impact damage created on brittle target materials by relatively incompressible projectiles has been studied. The damage obtained above the fracture threshold has been characterized, by detailed examination of (i) the extent of the radial fracture that develops early in the impact cycle, and (ii) the depth of the lateral fractures that form in the latter stages of the impact. The damage has then been analyzed by developing postulates based on a dynamic stress analysis and quasi-static indentation data. The analysis has been used to show that the extent of the radial fracture depends primarily on the toughness of the target and the velocity and radius of the projectile; while the depth of the lateral fracture depends largely on the hardness of the target and the velocity, radius and density of the projectile.

The characterization of the impact fracture has been used to discuss the strength degradation and erosion in the fracture controlled regime. Comparison of the predicted behavior with available data have been encouraging, and indicate that further studies, with the present theme, could fully characterize the degradation and erosion phenomena.

7.0 ACKNOWLEDGEMENT

APPENDIX

Quasi-Static Fracture Analysis For Elastic Impact

The fracture under quasi-static elastic indentation is uniquely related to the peak force, P_m, by;[1]

$$C_c^{3/2} = A_1 \frac{P_m}{K_c} \tag{A1}$$

where C_c is the crack length and A_1 is a constant. But the peak force is related to the projectile and target properties by;[15]

$$P_m \approx A_2 R_p^2 v_o^{6/5} \rho_p^{3/5} / (E_p + E_t)^{2/5} \tag{A2}$$

where E is Young's modulus. Combining eqns (A1) and (A2) gives

$$C_c \approx A_3 \frac{v_o^{12/15} R_p^{4/3} \rho_p^{6/15}}{K_c^{2/3} (E_p + E_t)^{4/15}} \tag{A3}$$

REFERENCES

1. B. R. Lawn and T. R. Wilshaw, Jnl. Mater. Sci., 10 (1975) 1049.

2. A. G. Evans and T. R. Wilshaw, Acta Met., 24 (1976) 939.

3. A. G. Evans and T. R. Wilshaw, Jnl. Mater. Sci., in press.

4. A. G. Evans and E. A. Charles, Jnl. Amer. Ceram. Soc., 59 (1976) 371.

5. M. E. Graham, J. D. Carlyle and T. L. Menna, Review of Sci. Inst. 46 (1975) 1221.

6. M. E. Gulden and A. G. Metcalf, 'Study of Erosion Mechanisms of Engineering Ceramics', Solar Report No. RDR 1778-4, prepared under Contract N00014-73-C-0401, NR032-542 (April 1976).

7. M. L. Wilkins, UCRL-7322, Rev. 1 (Jan. 1969).

8. W. Goldsmith, Impact (Arnold, London) 1960.

9. H. Kolsky, Stress Waves in Solids (Dover, N.Y.) 1963.

10. G. C. Sih, Handbook of Stress Intensity Factors, Lehigh Univ. Press, 1973.

11. R. M. Blowers, J. Inst. Maths Applics, 5 (1969) 167.

12. J. W. Goodier, Proceedings of Seventh Hypovelocity Impact Symposium, Vol. 111 (1965) p. 215.

13. B. R. Lawn, to be published.

14. S. M. Wiederhorn and B. R. Lawn, Jnl. Amer. Ceram. Soc., to be published.

15. A. G. Evans, Jnl. Amer. Ceram. Soc., 56 (1973) 405.

TABLE I

Physical Properties of Target and Projectile Materials

MATERIAL	ACOUSTIC IMPEDANCE ($Kg\ m^{-2}s^{-1}$)	TOUGHNESS ($MPa\sqrt{m}$)	YOUNG'S MODULUS (GPa)	HARDNESS (GPa)	COMMENTS
ZnS (T)*	2.2×10^7	1.0	102	1.9	C.V.D.
MgO (T)	3.3×10^7	1.2	310	9.2	Fine grained, hot pressed
MgF_2 (T)	3.2×10^7	0.9	170	5.8	Hot pressed, fine grained
$MgAl_2O_3$ (T)	3.1×10^7	1.6	290	16.0	Coarse grained, sintered
Si_3N_4 (T)	3.2×10^7	5	320	16.0	Hot pressed
WC (T,P)	10.4×10^7	13	700	18.6	Bonded with 12% cobalt
GLASS (P) (QUARTZ)	1.6×10^7	~ 0.7	95	6.2	
SiC (P)	3.7×10^7	~ 3.0	420	23.0	

* T refers to target material and P refers to projectile material

TABLE II

Summary of Radial Fracture Results

TARGET MATERIAL	PROJECTILE MATERIAL	PROJECTILE RADIUS (µm)	PROJECTILE VELOCITY (ms^{-1})	AVERAGE RADIAL CRACK LENGTH (µm)
ZnS	WC	200 (sphere)	130	380
			230	590
			520	1600
			800	2300
		500 (sphere)	170	3400
	GLASS (QUARTZ)	500 (sphere)	160	2300
			350	4200
		190 (angular)	190	380
			105	230
			24	45
		53 (angular)	223	72
			125	30
	ALUMINA	26 (angular)	255	35
			138	18
MgO	WC	200 (sphere)	500	1800
	QUARTZ	190 (angular)	190	300
			105	170
MgAl$_2$O$_4$	WC	200 (sphere)	500	1500

(CONTINUED)

TABLE II - (Continued)

TARGET MATERIAL	PROJECTILE MATERIAL	PROJECTILE RADIUS (μm)	PROJECTILE VELOCITY (ms^{-1})	AVERAGE RADIAL CRACK LENGTH (μm)
MgF$_2$	SiC	560 (angular)	137	1600
			114	1300
			89	1100
			62	750
			33	350
Si$_3$N$_4$	SiC	560 (angular)	137	550
			68	300
	WC	200 (sphere)	640	340
WC	WC	200 (sphere)	650	150

TABLE III

Summary of Lateral Crack Depth Results

TARGET MATERIAL	PROJECTILE MATERIAL	PROJECTILE RADIUS (μm)	PROJECTILE VELOCITY (ms^{-1})	AVERAGE DAMAGE DEPTH (μm)
ZnS	WC		860	595
		200	520	350
			130	270
		500	170	800
	GLASS (QUARTZ)	190	190	140
		500	350	780
MgO	WC	200	500	280
	QUARTZ	190	190	90
MgF$_2$	SiC	560	137	430
			89	300
Si$_3$N$_4$	SiC	560	137	270
	WC	200	640	290

TABLE IV

APPROXIMATE FRACTURE THRESHOLDS FOR GLASS (QUARTZ) PROJECTILES

MATERIAL	PROJECTILE RADIUS (μm)	THRESHOLD VELOCITY (ms^{-1})
ZnS	26	80
	55	40
	190	< 10
MgO	190	100
Si$_3$N$_4$	500	> 1000

TABLE V

EROSION DATA AND PHYSICAL PROPERTIES FOR FOUR CERAMIC

MATERIALS IMPACTED BY 115 μm QUARTZ PARTICLES

MATERIAL	PROJECTILE VELOCITY (ms^{-1})	MATERIAL REMOVAL PER IMPACT (m^3)	K_c (MPa$\sqrt{m}$)	H [+] (GNm^{-2})	z (kg m^{-2}s^{-1})
MgF$_2$	98	4.9×10^{-15}	0.9	5.8	3.2
	140	9.7×10^{-15}			
	180	-----			
Reaction Sintered Si$_3$N$_4$	98	1.3×10^{-15}	2.2	3.3	2.0
	140	1.9×10^{-15}			
	180	2.5×10^{-15}			
Al$_2$O$_3$ (Alsi Mag)	98	8.6×10^{-17}	4.1	12	4
	140	9.9×10^{-17}			
	180	2.7×10^{-16}			
Hot Pressed Si$_3$N$_4$	98	3.6×10^{-18}	5.0	16	3.2
	140	9.1×10^{-18}			
	180	1.5×10^{-17}			

[+] The hardnesses are the quasi-static Vickers hardness in the macro-indentation load independent regime.

FIGURE CAPTIONS

Fig. 1. Typical impact damage patterns observed in the plastic response regime
for ZnS impacted by WC: (a) is scanning electron micrograph illustrating
the central plastic impression, the radial cracks and the lateral cracks
that have caused material to be removed; (b) is a reflected light micro-
graph of the same impact which provides a clearer view of the radial
crack, (c) is a polarized reflected light micrograph of the same impact
illustrating the symmetry of the lateral fracture; (d) is a scanning
electron micrograph of a higher velocity impact showing the greater
intensity of the lateral fracture and the partial removal of the plastic
impression.

Fig. 2. Interference optical micrographs of the impact damage on MgF_2 created
by angular SiC projectiles, (a) illustrates the interaction between
adjacent impacts, and (b) shows the asymmetry of the fracture.

Fig. 3. Polarized reflected light micrographs of the impact damage on ZnS
created by angular quartz projectiles, (a) shows the damage to an as-
polished surface and indicates (at position A, for example) the lack
of interaction   for quite closely separated impacts, and (b)
illustrates the damage to a pre-eroded surface.

Fig. 4. The impact damage on MgO created by angular quartz projectiles: (a) is
a transmission optical micrograph, and (b) is a scanning electron
micrograph of the same impact formed at low velocity; (c) is a polarized
transmission light micrograph of an impact created at intermediate
velocity   (105 ms^{-1}); (d) is a scanning electron micrograph of an
impact generated at a higher velocity (190 ms^{-1}).

Fig. 5.   Optical reflected light micrographs of orthogonal sections through ZnS targets impacted by WC and glass projectiles: (a) indicates the extent of the radial and lateral fracture for a WC projectile target; (b) shows the same impact but highlights the formation of lateral cracks from radial cracks; (c) illustrates the extent of the radial and lateral fracture for a glass projectile impact; (d) is the same as (c) but indicates the zone of microfracture beneath the center of impact.

Fig. 6.   A transmitted light micrograph of an orthogonal section through an MgO target impacted by quartz projectiles indicating a lateral crack and the profile of a radial crack.

Fig. 7.   A plot of the radial crack length C_r, normalized by the projectile velocity v_0, as a function of the projectile velocity.

Fig. 8.   A comparison of the radial crack length for dynamic and quasi-static penetration in ZnS and MgF_2.

Fig. 9.   The variation in the depth of lateral fracture, h, with the impression radius, a, for ZnS impacted by a variety of projectiles.

Fig. 10.   An optical reflected light micrograph of the damage on hot pressed silicon nitride created by a 1000 μm glass sphere at 500 ms^{-1}; note the absence of fracture.

Fig. 11.   The contact parameters for the impact of a ZnS target by a 400 μm WC projectile at 860 ms^{-1}, (a) the time dependence of the contact pressure, (b) the time dependence of the contact radius.

Fig. 12.   The growth of the plastic zone during the penetration of a ZnS target impacted by a 400 μm WC projectile at 860 ms^{-1}, (a) at .083 μs, (b) at .15 μs.

Fig. 13. The tensile stresses generated during the impact of a ZnS target by a 400 μm WC projectile, (a) the in-plane tensile stresses during penetration (860 ms^{-1} projectile at .15 μs), (b) the out-of-plane tensile stresses during penetration (860 ms^{-1} projectile at .15 μs), (c) the in-plane tensile stresses during rebound (200 ms^{-1} projectile), (d) the in-plane tensile stresses after rebound (200 ms^{-1} projectile).

Fig. 14. A plot of the normalized radial crack length, C_r/v_o, as a function of the projectile radius, R_p, for four target materials with similar impedance and toughness, and for a range of projectiles.

Fig. 15. The normalized radial crack lengths for Si_3N_4 and WC targets, compared with the data line from Fig. 14.

Fig. 16. A plot of the normalized penetration, q/R_p, for two values of target density and work hardening exponent.[12]

Fig. 17. The dependence of the normalized lateral crack depth, h/R_p, on the parameter, $v_o \sqrt{\rho_p}/H$, for a range of target and projectile materials.

Fig. 18. The effect of projectile velocity on the retained strength parameter $\sigma_R v_o^{0.5} R_p^{0.8}$ for glass targets impacted by WC spheres.[14]

Fig. 19. A plot of the normalized material removal per particle for four targets impacted by quartz particles, as a function of the prime target variable $(1/K_c^5 H)$.

RADIAL CRACKS

PLASTIC IMPRESSION

LATERAL CRACKS

100μm

200μ

Figure 1

INTERACTION ZONE

1000μ
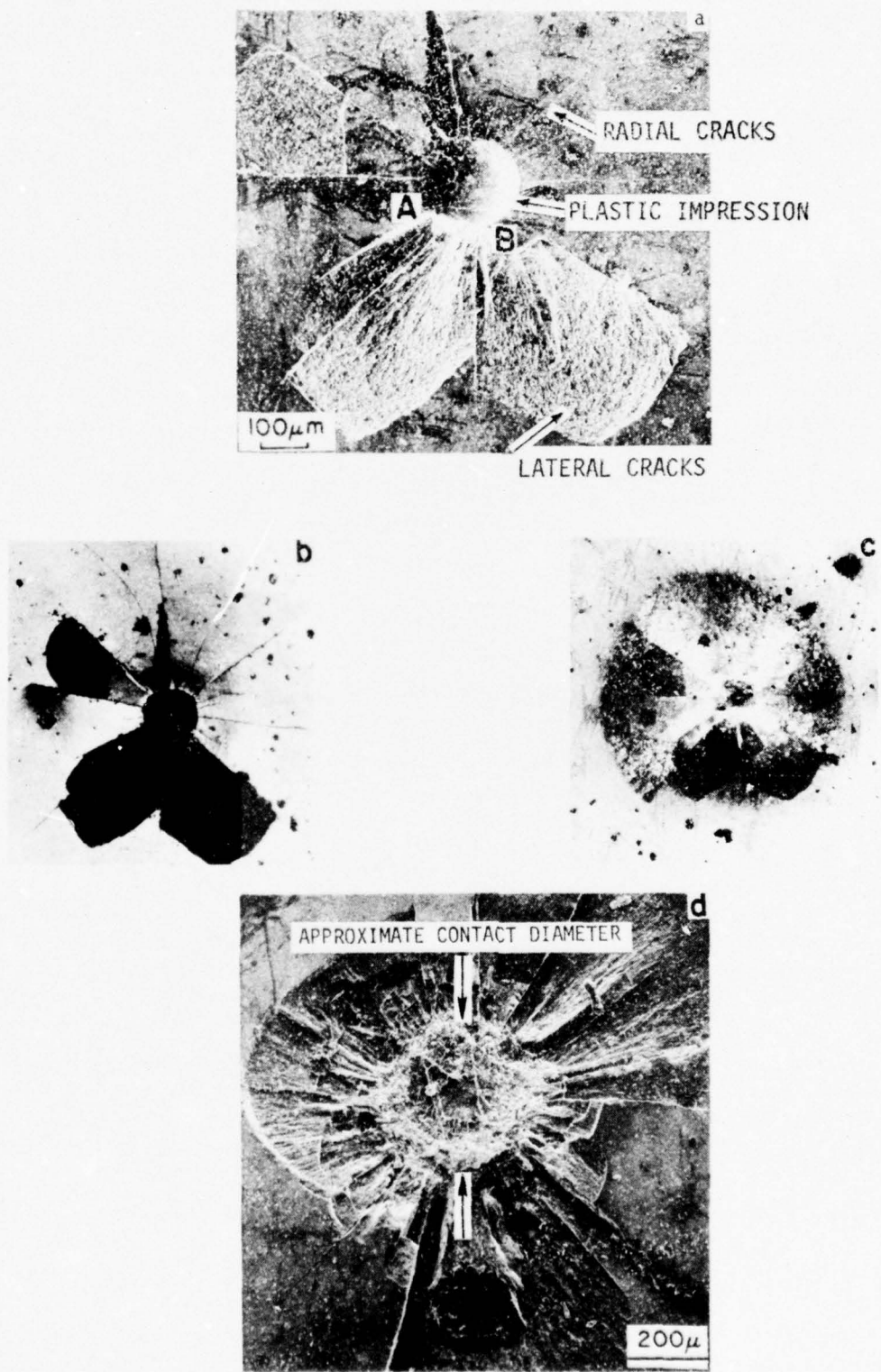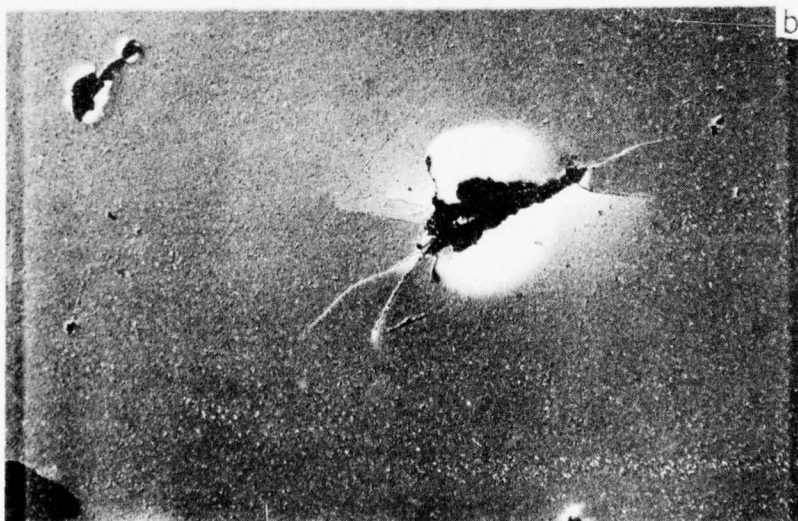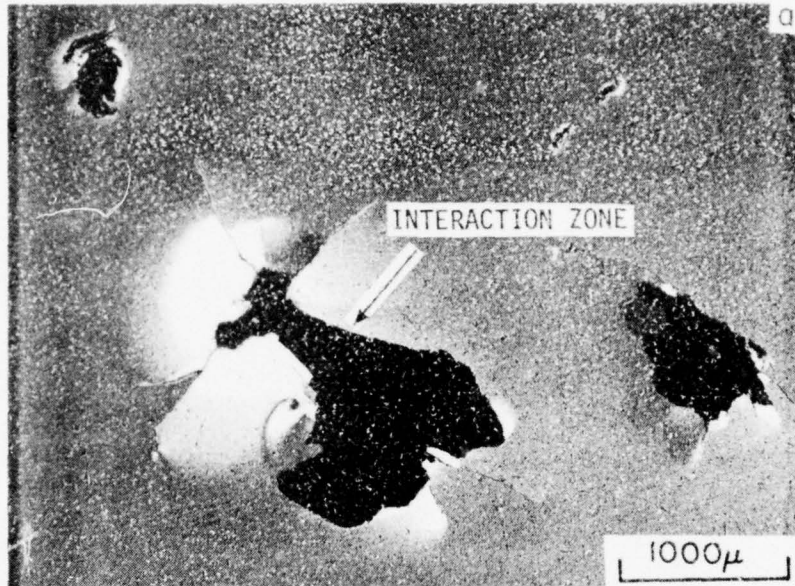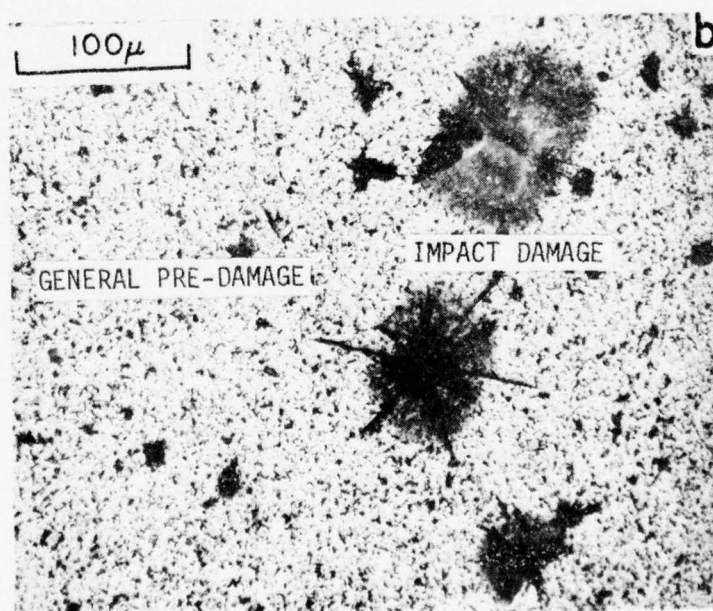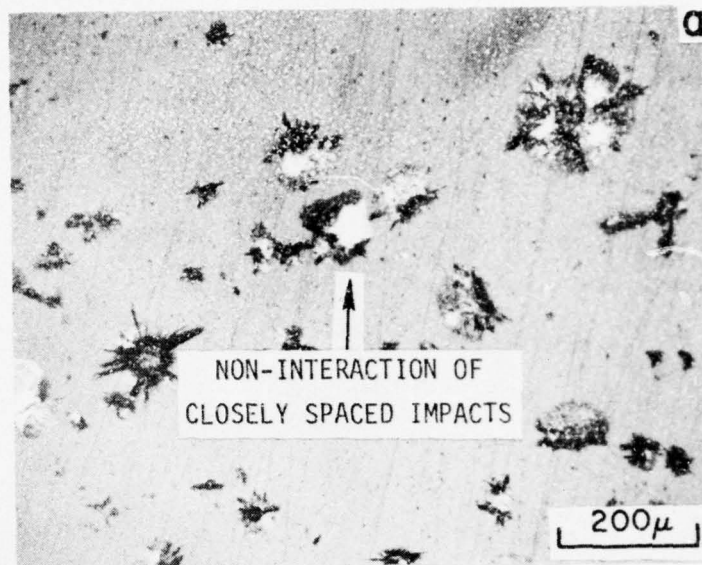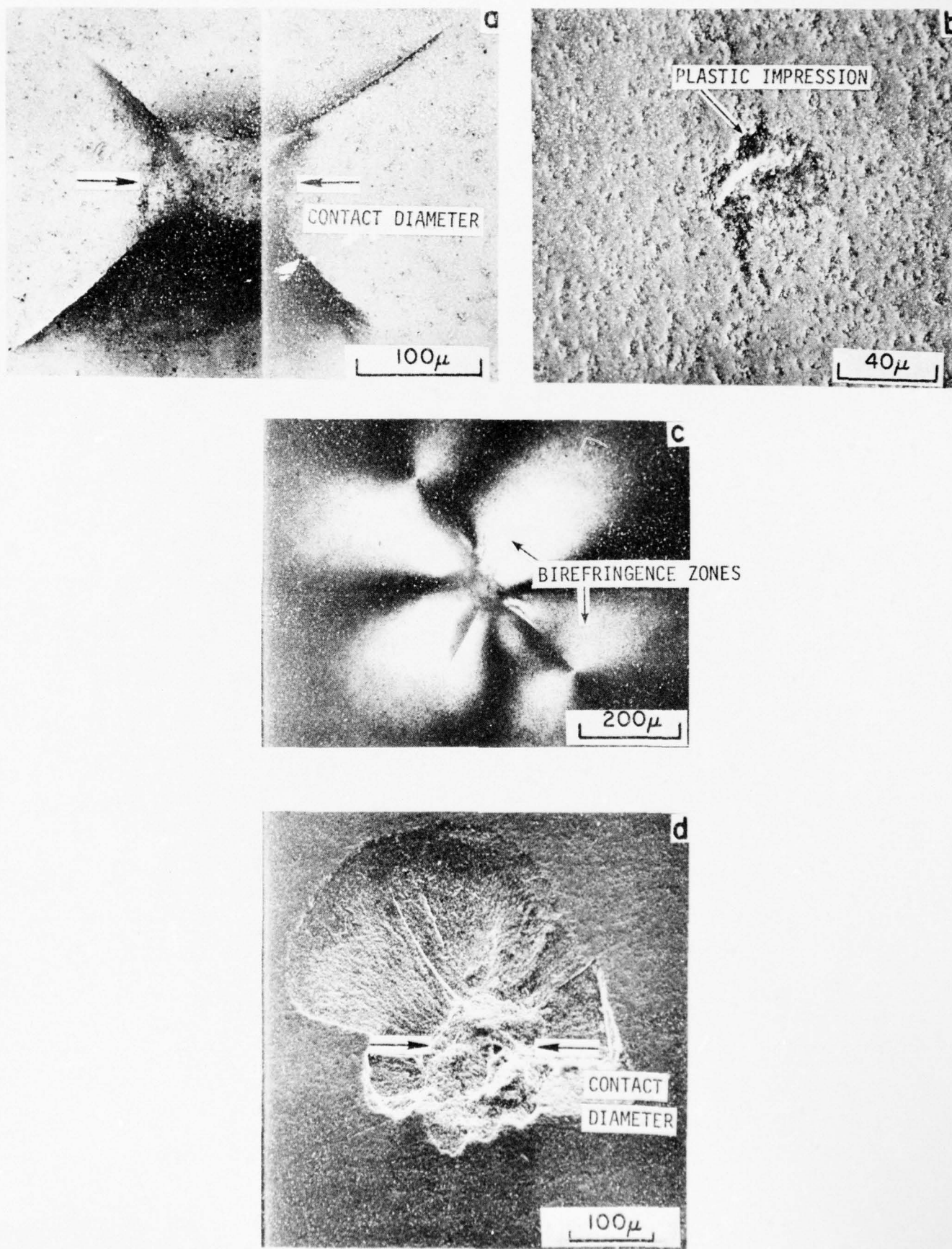
Figure 2

Figure 3

Figure 4
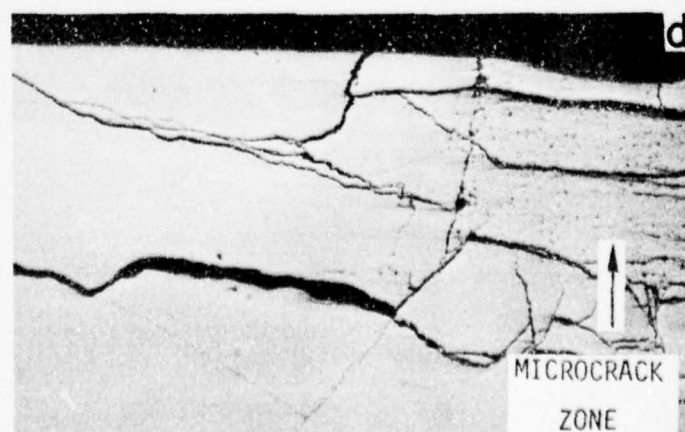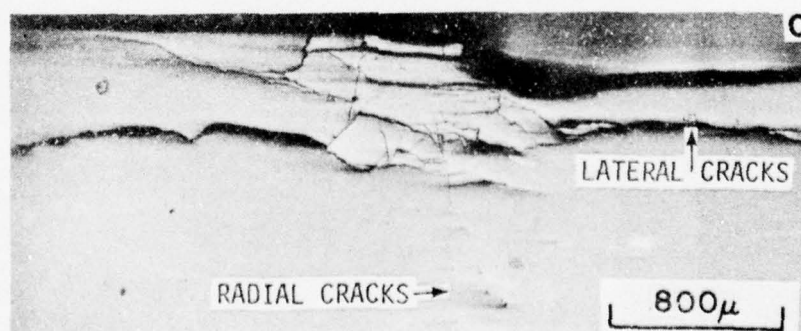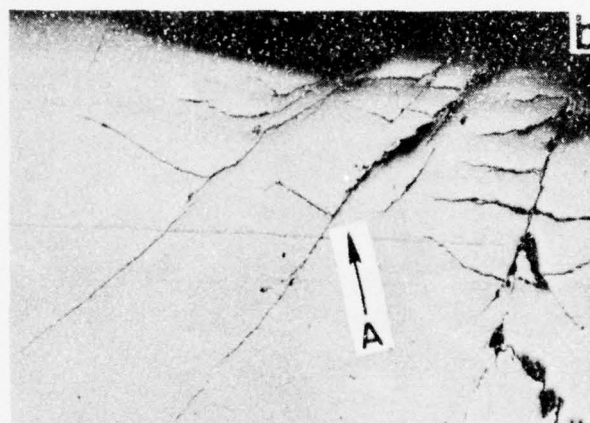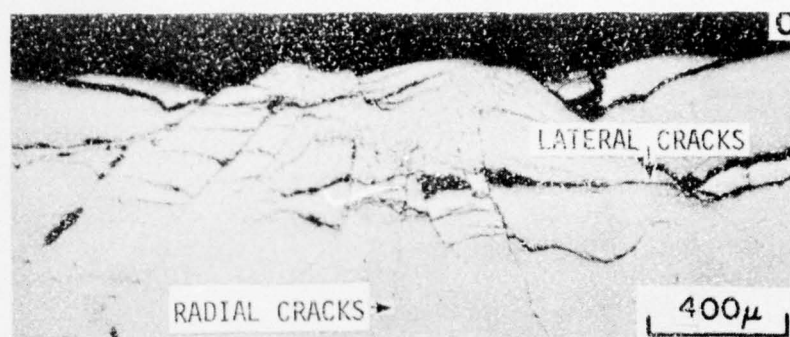
Figure 5
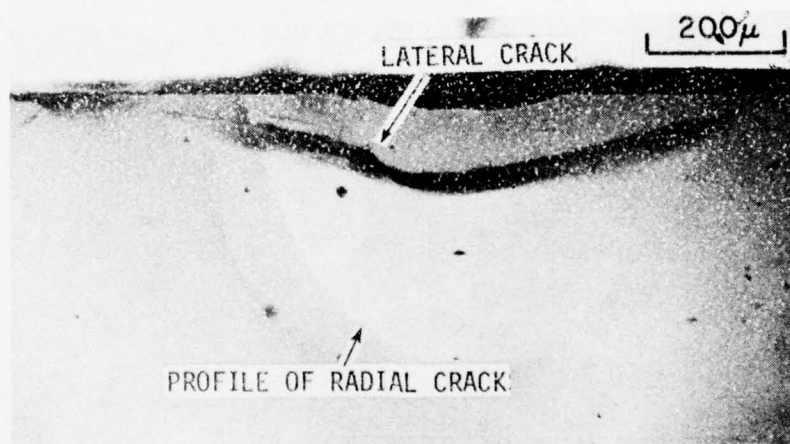
Figure 6
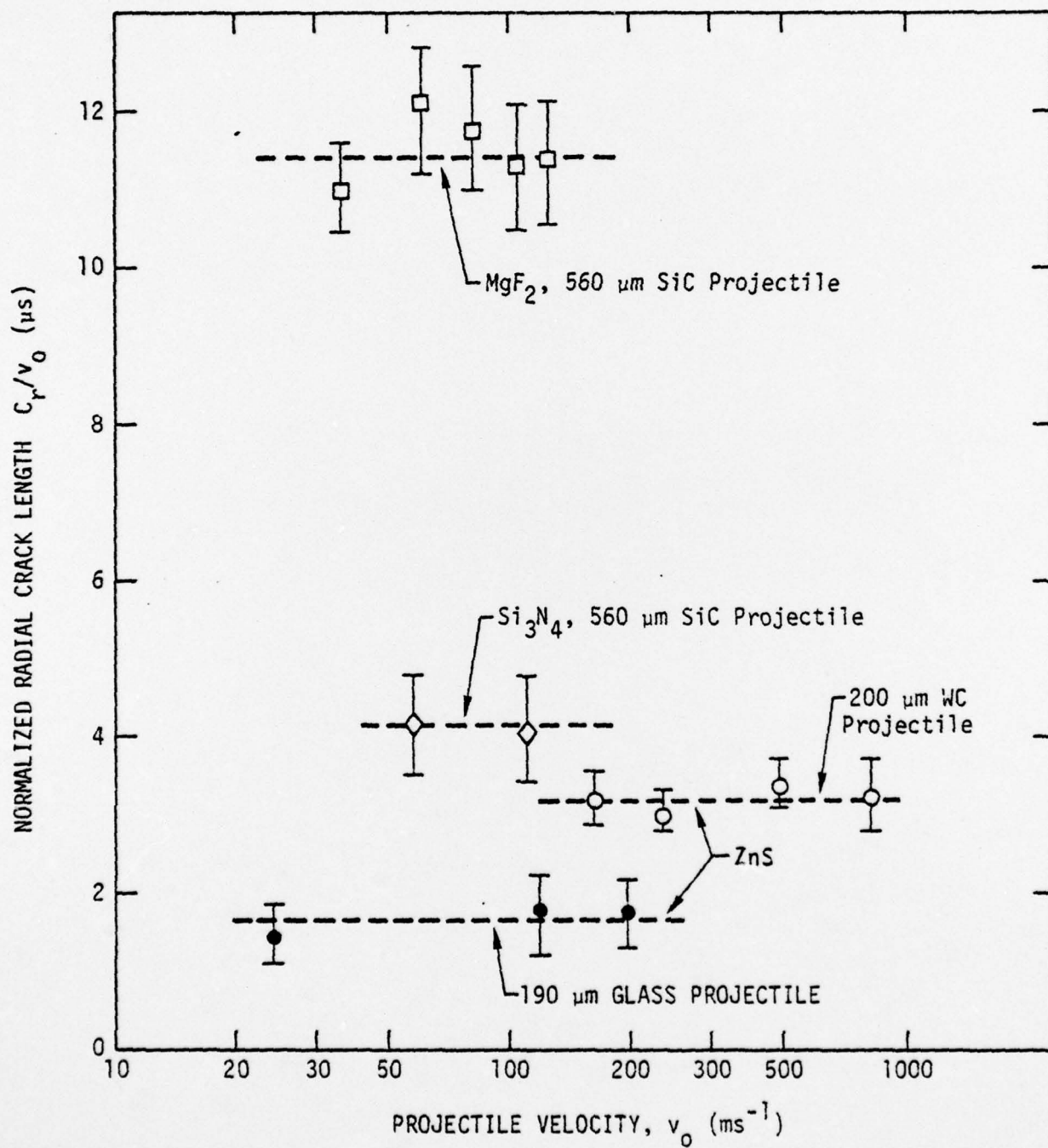
Figure 7
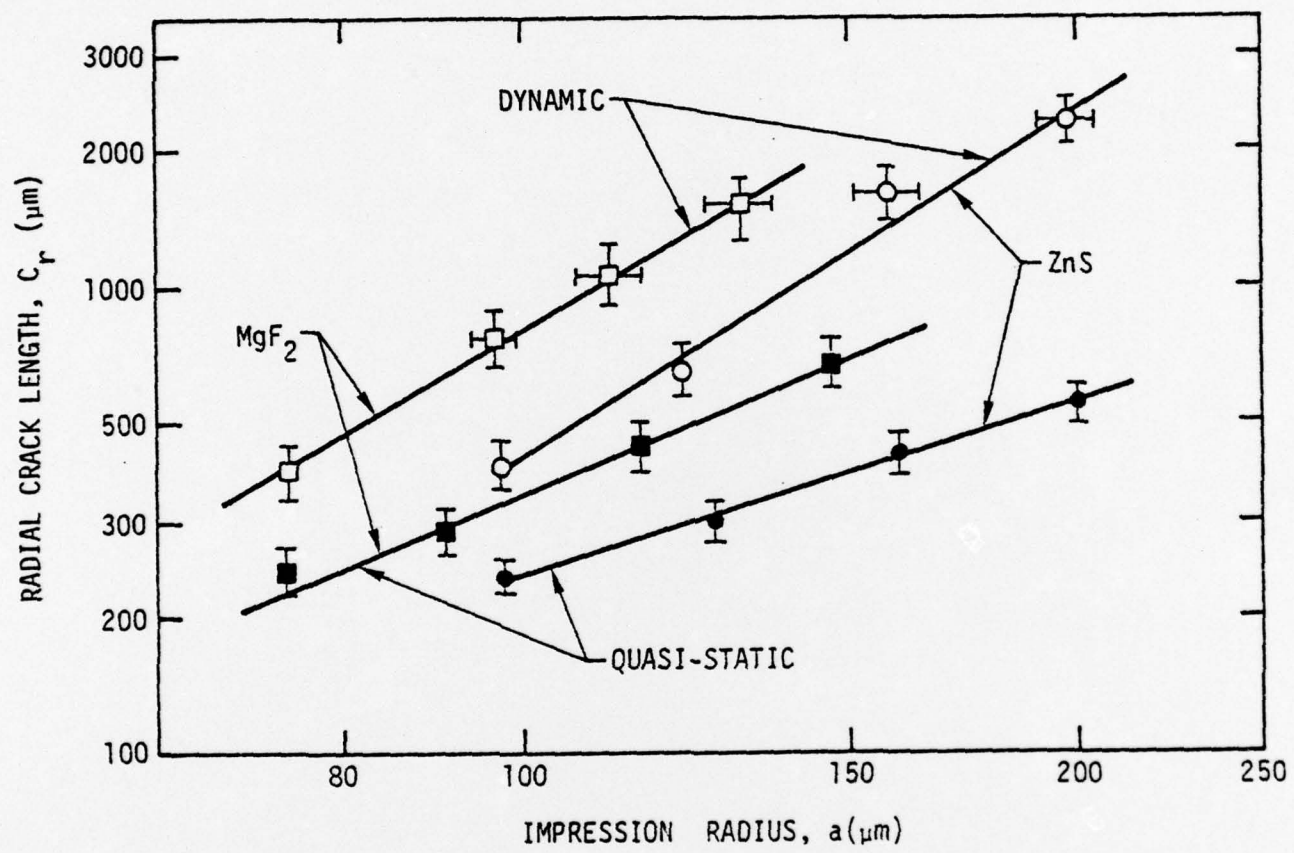
Figure 8
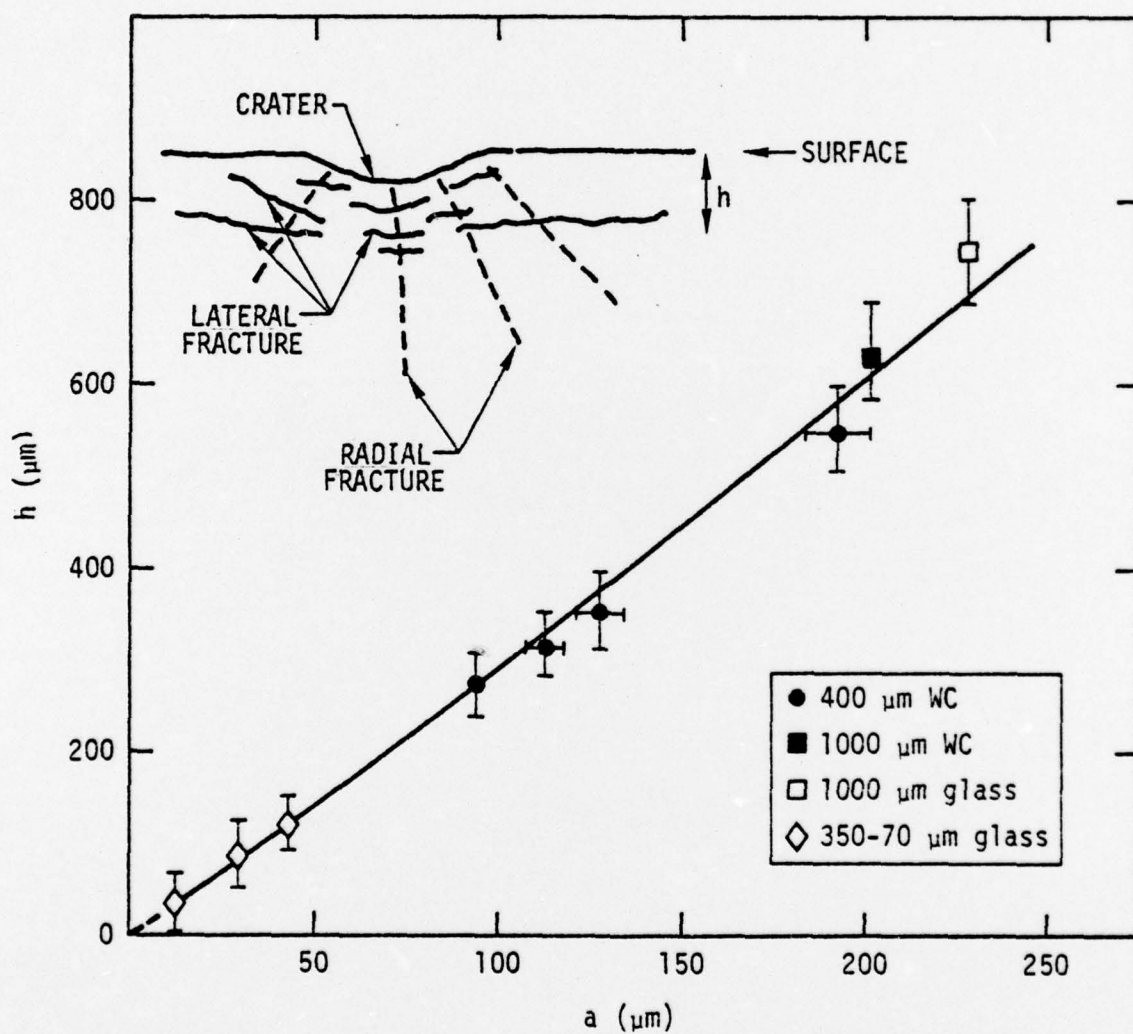
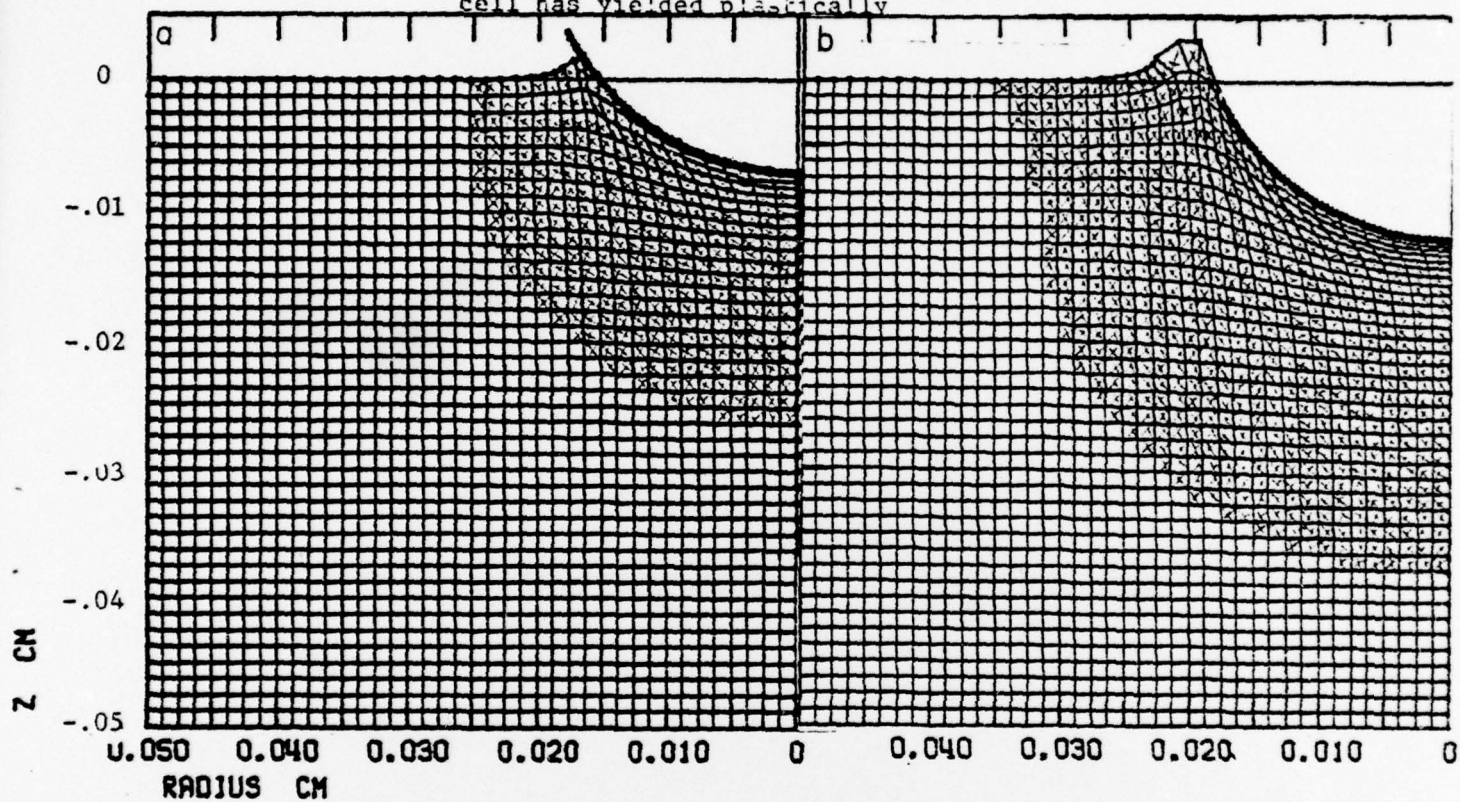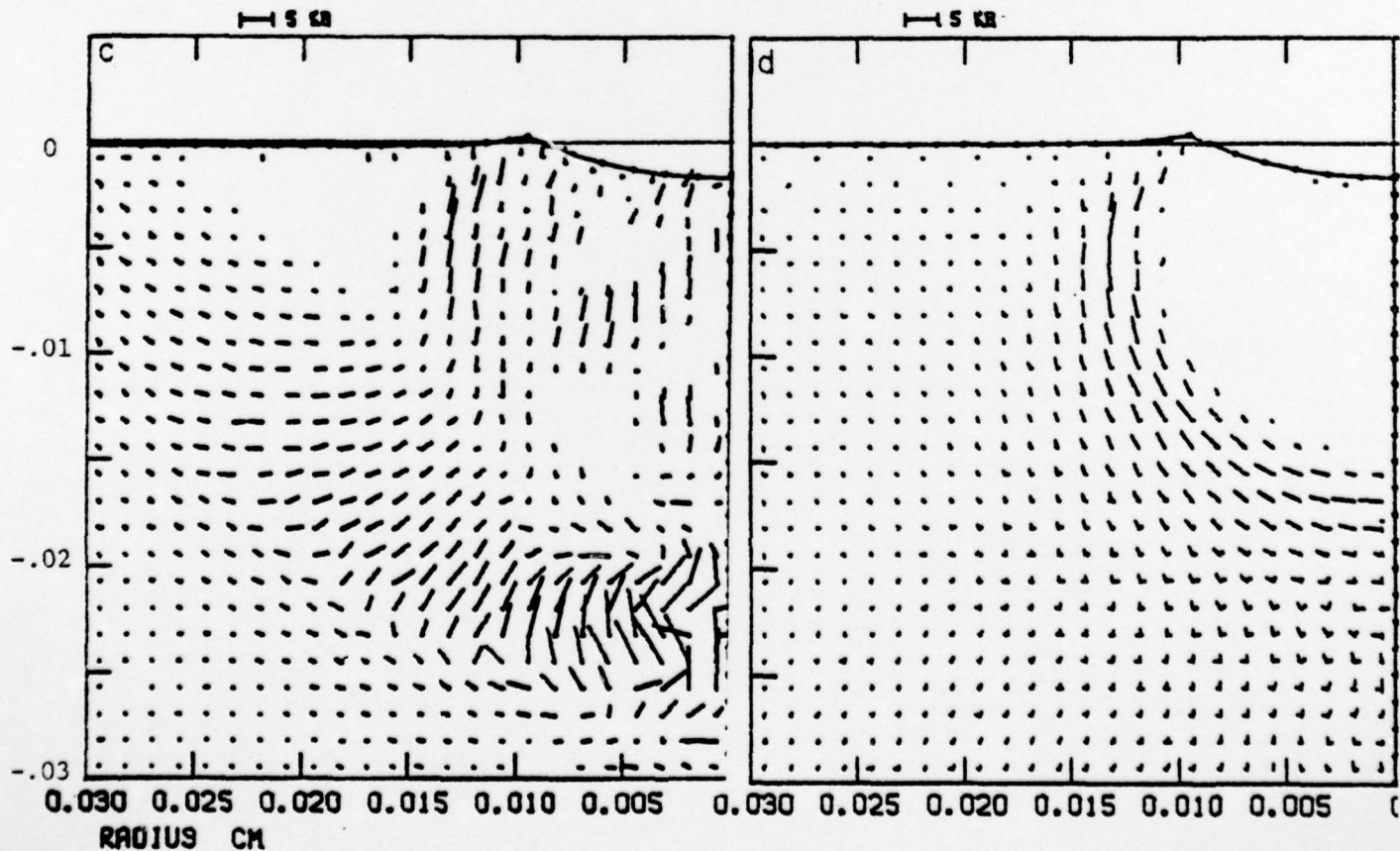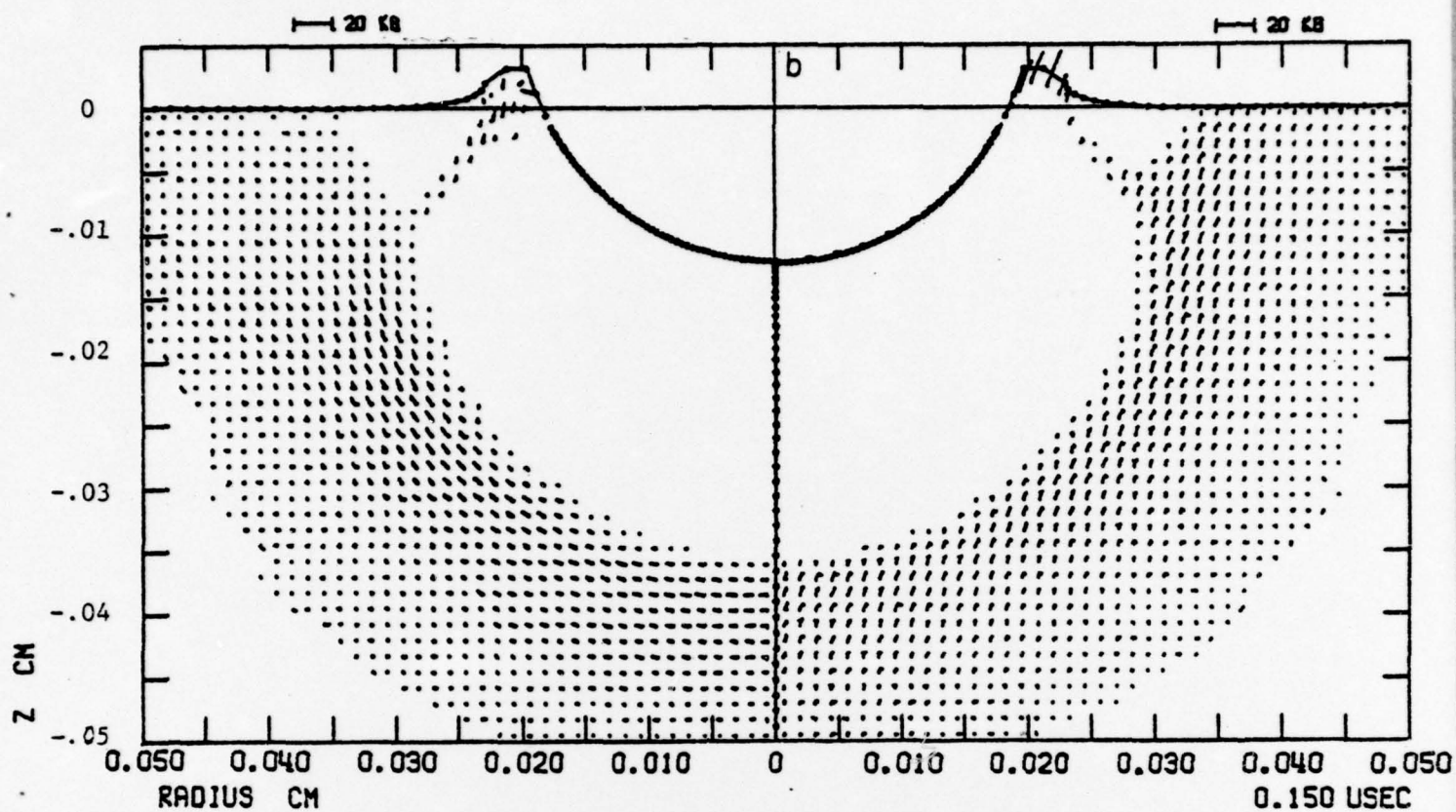Figure 9

200μ
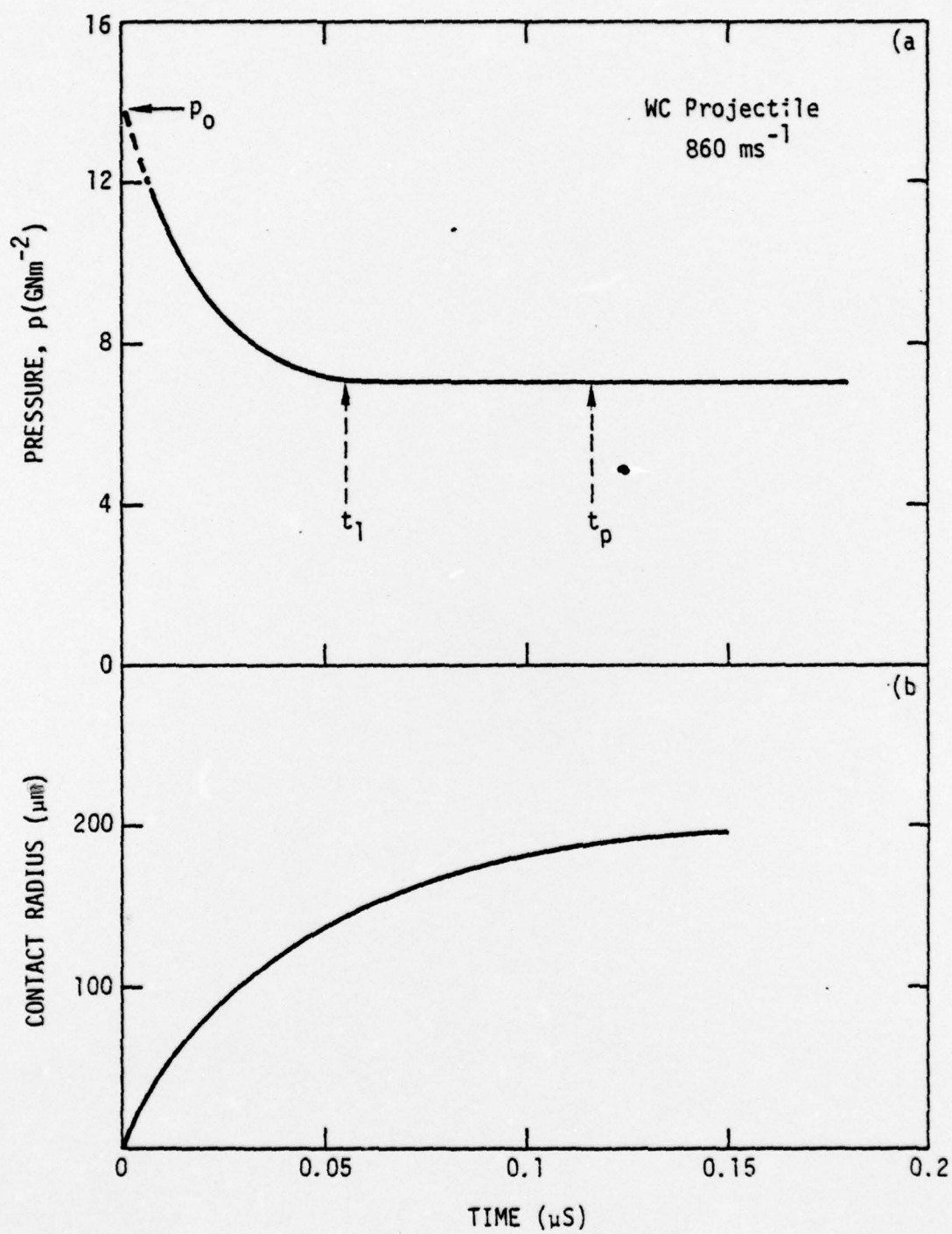
Figure 10

Figure 11
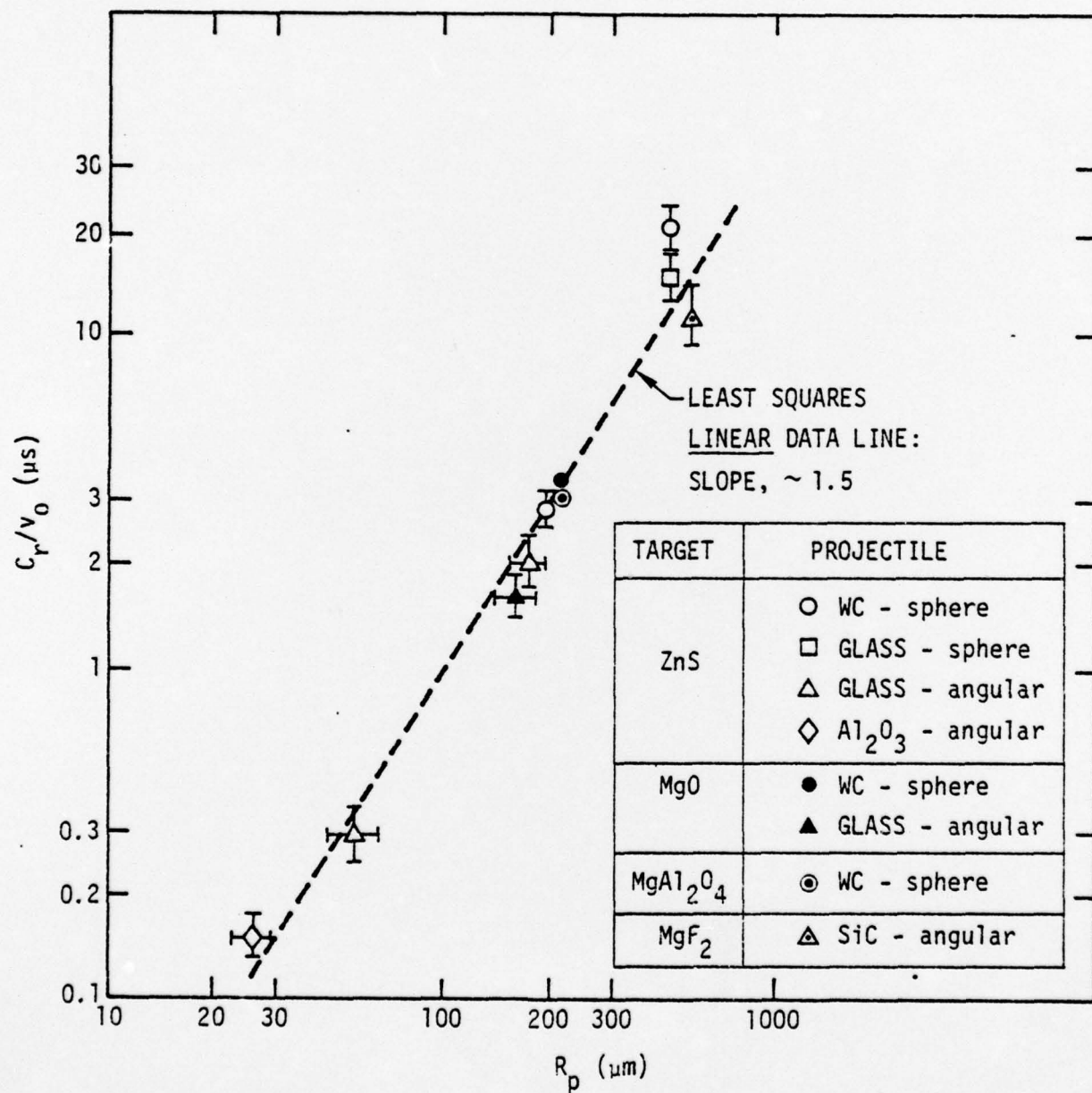
Figure 12

Figure 13

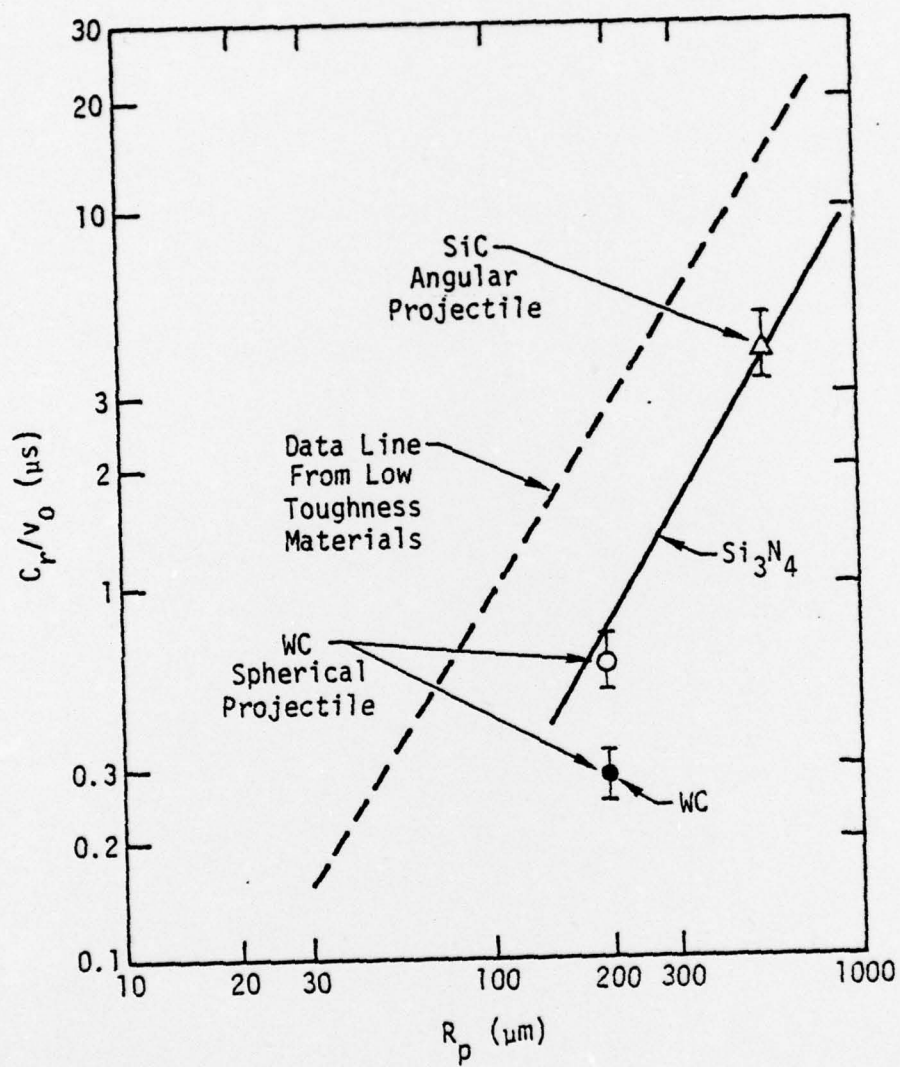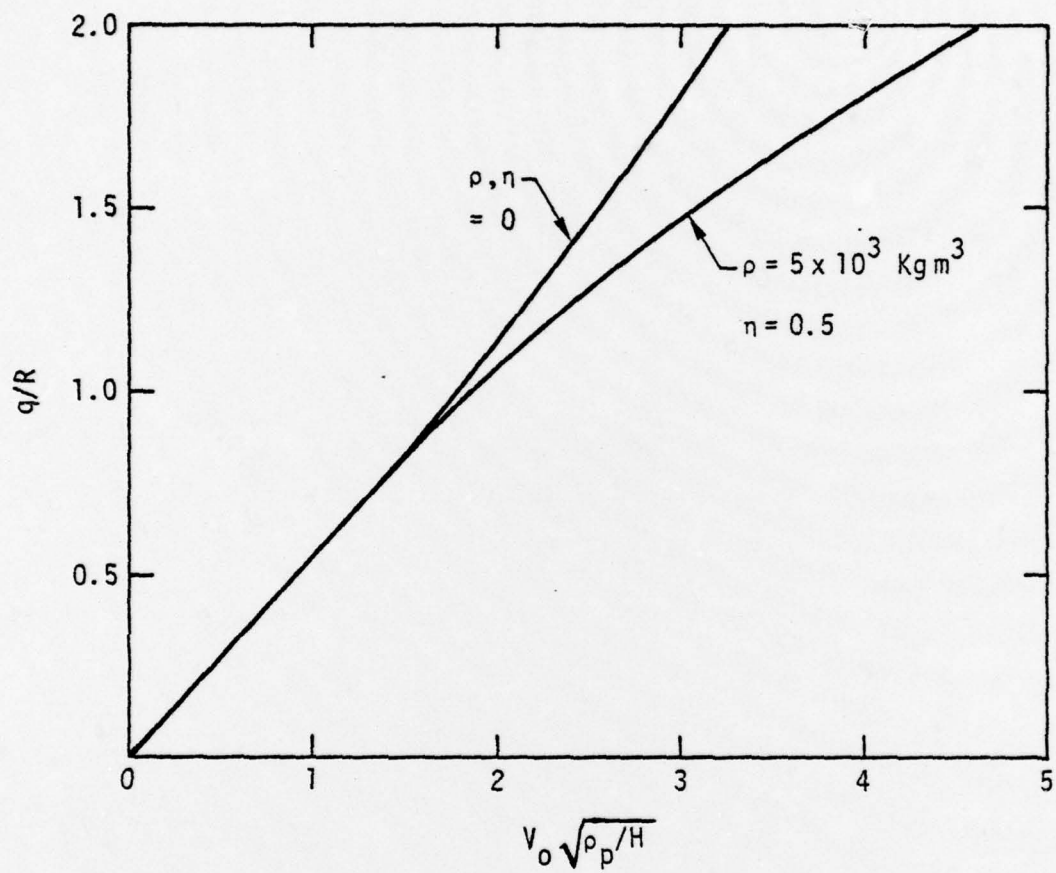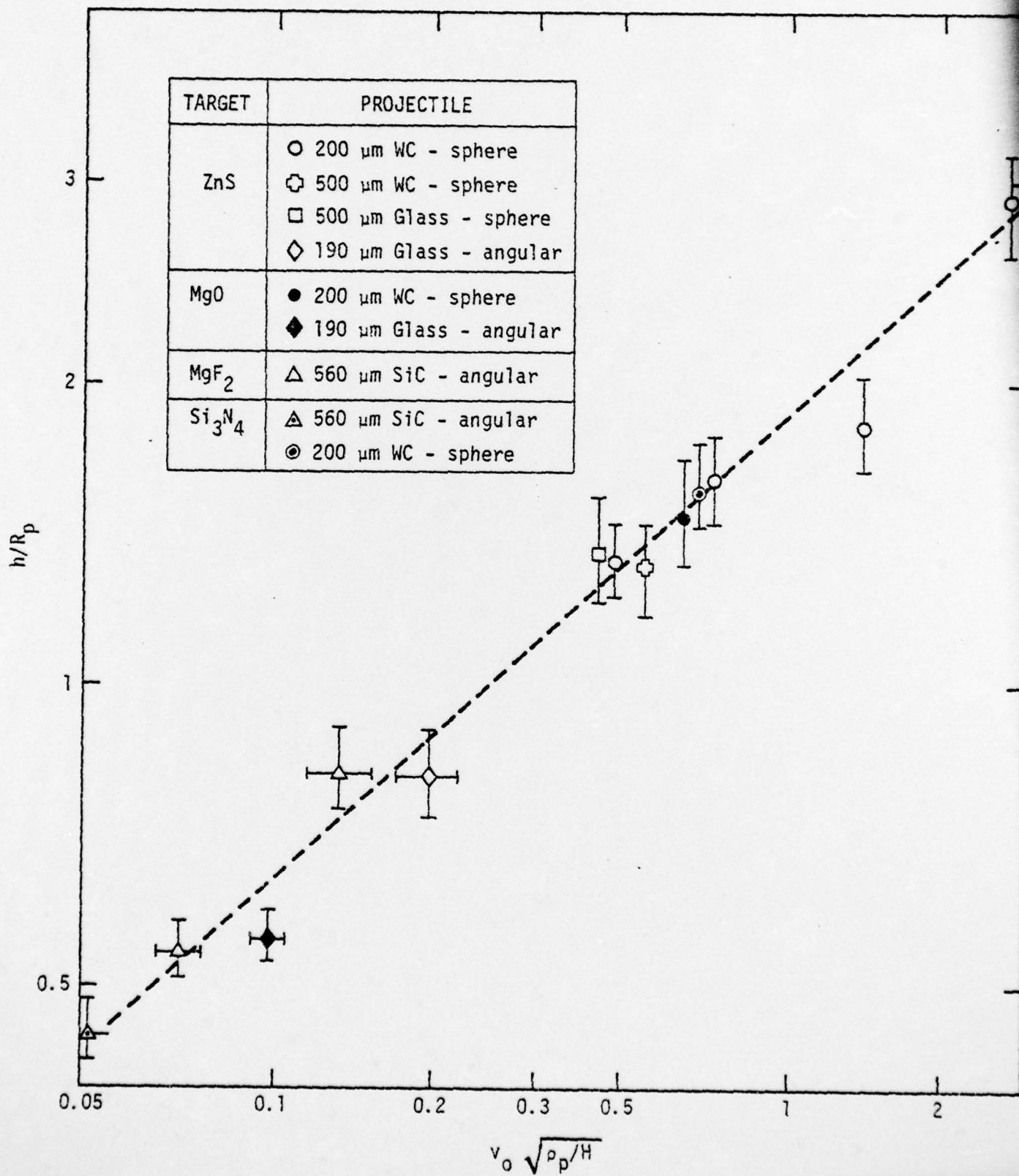Figure 14

The radial crack length for a range of ceramic target materials.
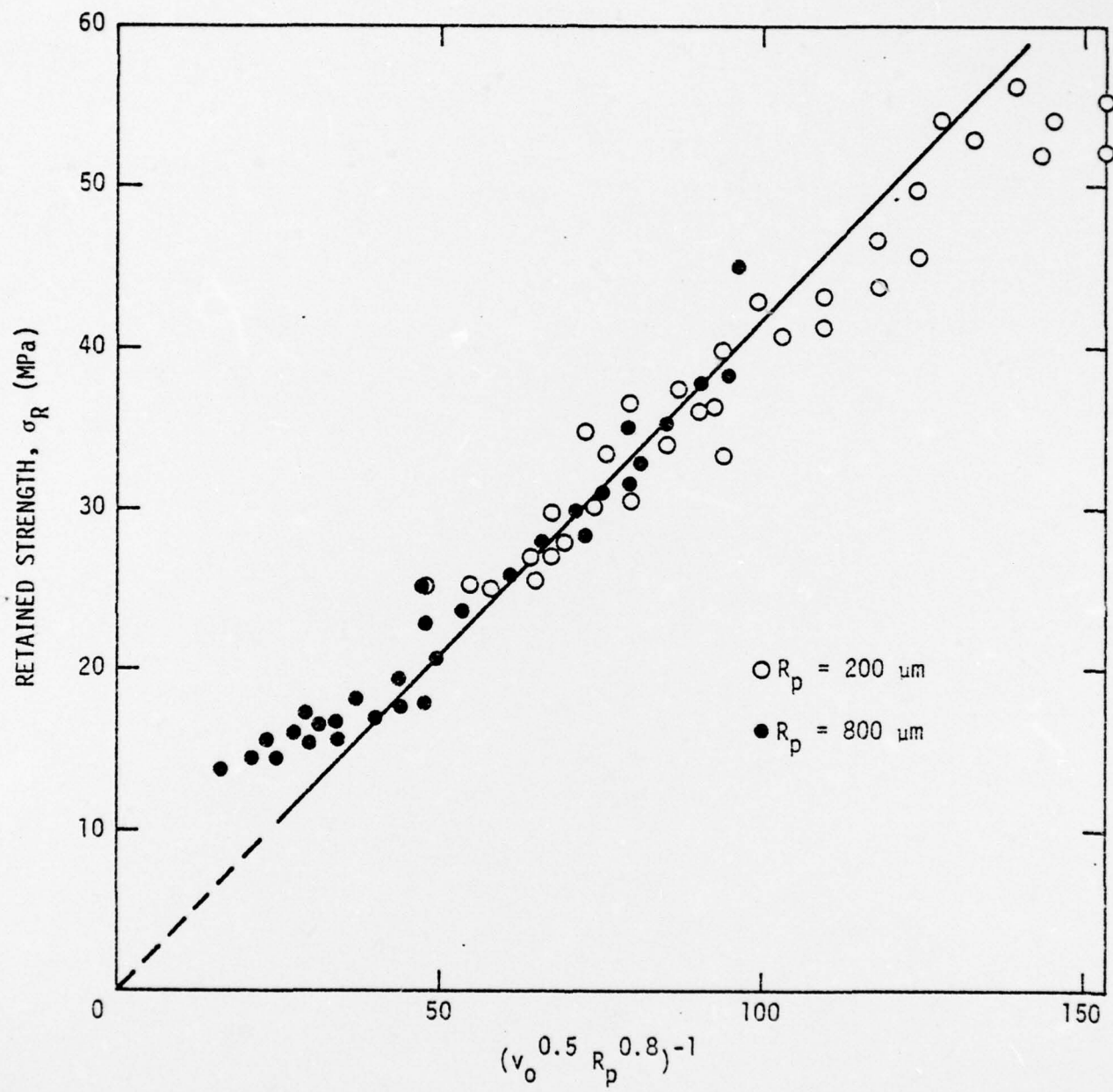
Figure 15

Figure 16

Figure 17

Figure 18

Figure 19